Earth and Planetary Science Letters 415 (2015) 54–66

Contents lists available at ScienceDirect

Earth and Planetary Science Letters

www.elsevier.com/locate/epsl

The effects of sulfur, silicon, water, and oxygen fugacity on carbon solubility and partitioning in Fe-rich alloy and silicate melt systems at 3 GPa and 1600 °C: Implications for core–mantle differentiation and degassing of magma oceans and reduced planetary mantles

Yuan Li *, Rajdeep Dasgupta, Kyusei Tsuno

Department of Earth Science, Rice University, 6100 Main Street, MS 126, Houston, TX 77005, USA

ARTICLE INFO

Article history:
Received 18 July 2014
Received in revised form 13 January 2015
Accepted 17 January 2015
Available online 9 February 2015
Editor: B. Marty

Keywords:
carbon partitioning
carbon speciation
oxygen fugacity
magma ocean
Mars
the Moon

ABSTRACT

The partition coefficient of carbon between Fe-rich alloy melt and silicate melt, $D_C^{metal/silicate}$ and solubility of C–O–H volatiles in reduced silicate melts are key parameters that need to be quantified in order to constrain the budget and origin of carbon in different planetary reservoirs and subsequent evolution of volatiles in magma oceans (MO) and silicate mantles. In this study, three sets of graphite-saturated experiments have been performed at 3 GPa and 1600 °C to investigate the effects of oxygen fugacity (fO_2), sulfur, silicon, and water on the dissolution and partitioning of carbon between Fe-rich alloy melt and silicate melt. The results show that the presence of 0–5 wt% sulfur in alloy melt does not have considerable effect on carbon solubility (~5.6 wt%) in alloy melt, determined by electron microprobe, whereas the presence of 0–10 wt% silicon decreases the carbon solubility from ~5.6 wt% to 1.8 wt%. Carbon solubility (11–192 ppm) in silicate melt, determined by SIMS, is strongly controlled by fO_2 and the bulk water content. Decreasing $\log fO_2$ from IW-0.6 to IW-4.7 or increasing bulk water content from 0.07 to 0.55 wt% results in significant increase of carbon solubility in silicate melt. Raman and FTIR spectroscopic analyses of silicate glasses show that the carbon species is mostly methane, which is further confirmed by the strong, positive correlation between the non-carbonate carbon and non-hydroxyl hydrogen in silicate melt. The $D_C^{metal/silicate}$ ranging from 180 to 4600 decreases with decreasing fO_2 or increasing bulk water in silicate melt. In addition, increasing Si in alloy melt also decreases $D_C^{metal/silicate}$. Our results demonstrate that fO_2 and bulk water contents in silicate melt play an important role in determining the fractionation of carbon in planetary MO. A reduced, hydrous MO may have led to a considerable fraction of carbon retained in the silicate mantle, whereas an oxidized, dry MO may have lost almost its entire carbon into the core. If delivery of bulk Earth carbon predominantly occurred after >90% of accretion, i.e., in a relatively oxidized MO (IW-2 to IW-1), then with applicable $D_C^{metal/silicate} >$ 1000, most early Earth carbon would also enter the segregating core. Finally, the predominance of methane in reduced silicate melt with fO_2 below IW-1 also indicates that degassing of a hydrous, solidifying MO may have created a reduced early atmosphere, and degassing from lunar and Martian mantle may have released much more methane than carbon dioxide.

© 2015 Elsevier B.V. All rights reserved.

1. Introduction

Carbon, the fourth most abundant element in the Universe, has a significant effect on the planetary atmosphere composition, surface habitability, internal chemical differentiation, physical properties and dynamics (e.g., Eggler, 1976; Falloon and Green, 1989; Sleep and Zahnle, 2001; Zahnle et al., 2010; Stanley et al., 2011; Hirschmann, 2012; Dasgupta and Hirschmann, 2010; Dasgupta, 2013; Dasgupta et al., 2013a, 2013b; Sifré et al., 2014). Partition coefficient of carbon between alloy melt and silicate melt, $D_C^{metal/silicate}$ at conditions similar to a magma ocean (MO) is a key quantity that needs to be determined in order to constrain the origin and initial distribution of carbon between planetary silicate fraction and metallic core (Dasgupta, 2013; Chi et al., 2014). However, so far there are only a few studies that

* Corresponding author. Tel.: +1 713 348 5098.
E-mail address: Yuan.Li@rice.edu (Y. Li).

http://dx.doi.org/10.1016/j.epsl.2015.01.017
0012-821X/© 2015 Elsevier B.V. All rights reserved.

exclusively constrained the $D_C^{metal/silicate}$ relevant for MO (Dasgupta and Walker, 2008; Zhang and Yin, 2012; Dasgupta et al., 2013a; Chi et al., 2014). Only Dasgupta et al. (2013a), Stanley et al. (2014), and Chi et al. (2014) experimentally measured $D_C^{metal/silicate}$ (100–5000) as a function of temperature (1350–2100 °C), pressure (1–5 GPa), oxygen fugacity (~IW-0.4 to IW-1), silicate melt composition (NBO/T = 0.8–3.6), and alloy melt composition (Fe/Ni ratio). However, all of these studies constructed alloy melt compositions that either had carbon as the only light element (Dasgupta et al., 2013a; Stanley et al., 2014; Chi et al., 2014) or had only a minor presence of sulfur (Dasgupta et al., 2013a). Further, these experiments did not extend to very reducing conditions (<IW-1.5) that may be relevant for early accretion of terrestrial planets such as Earth (e.g., Wood et al., 2006).

Based on cosmochemical and geophysical consideration, and based on high-pressure experimental evidence, ~5–12% light elements mainly including carbon, oxygen, sulfur, and silicon have been proposed in the Earth's outer core to account for the core density deficit (e.g., Allegre et al., 1995; McDonough, 2003; Dasgupta and Walker, 2008; Bouhifd and Jephcoat, 2011; Wood et al., 2013). For instance, recent experimental studies suggested that 1–12 wt% sulfur and/or silicon could be in the Earth's core (Ricolleau et al., 2011; Morard et al., 2013; Siebert et al., 2013). The presence of sulfur, silicon, and carbon in alloy melt may significantly affect the partitioning of siderophile elements such as W, Mo, Ni, and Pb at P–T–fO_2 conditions of MO (Tuff et al., 2011; Bouhifd et al., 2013; Rai and van Westrenen, 2014). However, whether the presence of sulfur and/or silicon in alloy melt affect the partitioning of carbon remains unknown. Moreover, the effects of dissolved water in silicate melt and low fO_2 values (<IW-2) on $D_C^{metal/silicate}$ have never been investigated systematically. For example, the activity coefficient of carbon in alloy melt could be affected considerably with other interacting light elements in solution owing to strong non-ideal interactions of various light elements such as sulfur and carbon (Corgne et al., 2008; Dasgupta et al., 2009; Tsuno and Dasgupta, 2015) and silicon and carbon (Miettinen, 1998; Kawanishi et al., 2009). Hence one may expect that $D_C^{metal/silicate}$ will be considerably lower with higher S/C and/or Si/C ratios of alloy melt than what has been simulated so far in existing experiments.

Understanding the dissolution mechanism of carbon in silicate melt is also of great importance in understanding carbon solubility in silicate melt and thus magma's storage and transport capacities of carbon (Holloway et al., 1992; Kadik et al., 2004; Mysen et al., 2011; Stanley et al., 2011, 2014; Ardia et al., 2013; Dasgupta et al., 2013a; Chi et al., 2014). The species of C–H–O volatiles in reduced silicate melt, which are mainly a multifunction of fugacities of H_2O, H_2, and O_2, remain unclear, resulting in the carbon species degassed from reduced, solid planetary mantles such as those in Mars and the Moon remaining unclear and debated (Dasgupta, 2013; Wetzel et al., 2013; Stanley et al., 2014).

We therefore performed experiments investigating systematically (1) the effects of sulfur and/or silicon in Fe-rich alloy melt on C-solubility, (2) water in silicate melt, and log fO_2 ranging from ~IW-1 to IW-5 on C-solubility in silicate melt, and (3) carbon partitioning between alloy melt and silicate melt. All experiments were conducted at a constant pressure (3 GPa) and temperature (1600 °C) and at graphite-saturation. We also performed Raman and FTIR analyses in our silicate glasses to provide important constraints on the variation of the C–H–O species as a function of melt water content and log fO_2 down to ~IW-5.

Table 1
Chemical compositions of starting materials (in wt%).

Knippa	SiO_2	TiO_2	Al_2O_3	Cr_2O_3	FeO	MnO
	42.49	3.27	11.76	0.07	11.00	0.22
	MgO	CaO	Na_2O	K_2O	P_2O_5	Total
	12.33	11.59	3.05	2.03	0.83	99.66

Alloy mix	Fe	Ni	S	Si	Total
Fe–Ni–S					
S1	89.4	5.6	5	–	100
S2	91.4	5.6	3	–	100
S3	87.4	5.6	7	–	100
S4	84.4	5.6	10	–	100
Fe–Ni–Si					
Si1	91.4	5.6	–	3	100
Si2	89.4	5.6	–	5	100
Si3	87.4	5.6	–	7	100
Si4	84.4	5.6	–	10	100
Si5	76.4	5.6	–	18	100
Si6	79.4	5.6	–	15	100
Fe–Ni–S–Si					
SSi1	80.9	5.6	3.5	10	100
SSi2	77.9	5.6	3.5	13	100
SSi3	74.9	5.6	3.5	16	100

Knippa: a natural basanite that has been used in many high-pressure partitioning experiments (e.g., Righter et al., 2011; Chi et al., 2014). The major element composition of Knippa basanite was listed in Lewis et al. (1993).

2. Methods

2.1. Starting materials

Starting materials included ~60–70 wt% silicate powder of a natural basanite (Knippa) and 30–40 wt% metal powder of Fe–Ni–S, Fe–Ni–Si, or Fe–Ni–S–Si mixture. The natural basanite (Table 1) was dehydrated at 1000 °C and log fO_2 of ~FMQ-2 using a CO–CO_2 Deltech gas mixing furnace for 24 h in order to obtain a relatively low water content. In order to study the effects of silicon and sulfur in alloy melt on carbon partitioning thirteen homogeneous metal mixtures (Table 1) were prepared from analytical grade Fe, Ni, Si, and FeS powders. All the homogeneous mixtures of metal and silicate were stored in a desiccator at 100 °C for ≥24 h to remove completely the absorbed ethanol used for homogenization before loading into graphite capsules and subjecting to high P–T conditions.

2.2. High pressure–temperature experiments

Three sets of experiments were conducted to investigate factors that may potentially control carbon solubility and partitioning between alloy melt and silicate melt (Table 2): the first set in the Knippa–Fe–Ni–S system to investigate the effect of sulfur in alloy melt; the second set in the Knippa–Fe–Ni–Si system to investigate the effect of silicon in alloy melt; and the third set in the Knippa–Fe–Ni–S–Si system to investigate the effect of coexistence of sulfur and silicon in alloy melt. These three sets of experiments also allowed us to investigate the effects of fO_2 and water in silicate melt on solubility of C–O–H volatiles and carbon partitioning (see below).

All the experiments were conducted using an end-loaded piston cylinder device at 3 GPa and 1600 °C at the experimental petrology laboratory of Rice University, following assembly and calibration as given in Tsuno and Dasgupta (2011). Graphite capsule was used in order to study carbon solubility in silicate melt and alloy melt. The use of graphite capsule also allowed achieving temperatures that approach that of planetary magma oceans. Experiments were pressurized first at room temperature and then heated at the rate of 100 °C/min. In order to reduce porosity in the graphite capsules

Table 2
Summary of experimental conditions, quench products, estimates of volatile species abundance, and carbon partitioning.

Run no.	P (GPa)	T (°C)	Duration (h)	fO_2 (ΔIW[a])	fO_2 (ΔIW[b])	Starting material	Quench phases	Raman	FTIR C[c] (ppm) in SM	FTIR H_2O[d] (wt%) in SM	FTIR H_2O[d] (wt%) in SM	SIMS H_2O (wt%) in SM	NBO/T[e] in SM	H_2[f] (wt%) in SM	H_2[f] (wt%) in SM	SIMS C (ppm) in SM	C in AM (wt%)	$D^{metal/silicate}$
Knippa-Fe-Ni-S																		
G315-01	3	1600	2.0	−1.4	−0.64	Knippa + S1	AM + SM	√	X	X	X	0.22(0)	1.46			46(0)	5.88(39)	1291(86)
G316-02	3	1600	2.0	−1.5	−0.72	Knippa + S2	AM + SM	√	10(2)	0.23(1)	0.16(1)	0.34(1)	1.48	0.0122	0.02	55(1)	5.61(10)	1016(29)
G317-03	3	1600	2.5	−1.4	−0.59	Knippa + S3	AM + SM + SulfM	√	9(1)	0.31(0)	0.21(2)	0.47(3)	1.51	0.0178	0.0289	59(2)	5.81(25)	981(57)
G318-04	3	1600	2.0	−1.4	−0.70	Knippa + S4	AM + SM + SulfM	√	10(1)	0.34(1)	0.24(1)	0.55(1)	1.54	0.023	0.0341	65(1)	5.31(8)	820(17)
Knippa–Fe–Ni–Si																		
G319-05	3	1600	2.0	−2.0	−1.3	Knippa + Si1	AM + SM	√	n.d	0.19(0)	0.13(0)	0.25(1)	1.22	0.0063	0.0129	22(2)	5.53(15)	2480(216)
G320-06	3	1600	2.3	−2.2	−1.5	Knippa + Si2	AM + SM	√	n.d	0.21(1)	0.15(1)	0.25(0)	1.14	0.0048	0.0115	18(0)	5.58(15)	3042(94)
G321-07	3	1600	2.0	−2.9	−2.2	Knippa + Si3	AM + SM + Cpx	√	n.d	0.17(0)	0.12(0)	0.19(0)	0.97	0.0017	0.0073	12(1)	5.66(12)	4612(306)
G322-08	3	1600	2.0	−4.8	−4.2	Knippa + Si4	AM + SM + Cpx	√	n.d	X	X	0.68(0)	0.88			74(0)	5.07(17)	685(24)
G326-12	3	1600	2.0	−5.4	−4.7	Knippa + Si5	AM + SM	√	n.d	0.04(0)	0.03(0)	0.12(1)	0.81	0.0093	0.0104	24(2)	1.82(75)	753(315)
G329-15	3	1600	2.0	−5.1	−4.3	Knippa + Si6	AM + SM	√	n.d	0.03(0)	0.02(0)	0.07(0)	0.88	0.0039	0.0051	11(2)	4.54(19)	4214(646)
Knippa–Fe–Ni–S–Si																		
G330-16	3	1600	2.0	−5.0	−4.2	Knippa + SSi1	AM + SM	√	n.d	0.15(0)	0.1(0)	0.43(9)	0.89	0.0309	0.0365	96(4)	5.20(9)	540(22)
G331-17	3	1600	2.0	−5.2	−4.4	Knippa + SSi2	AM + SM	√	n.d	0.09(0)	0.07(0)	0.41(1)	0.88	0.036	0.0383	158(2)	5.02(11)	317(8)
G337-19	3	1600	3.0	−5.3	−4.6	Knippa + SSi3	AM + SM	√	n.d	0.05(0)	0.03(0)	0.35(1)	0.88	0.0338	0.036	192(1)	3.38(20)	176(11)

The fO_2 prevailing during the experiments was calculated using the equilibrium: FeO (silicate melt) = Fe (alloy melt) + $1/2O_2$, from which the fO_2 of the experiment relative to fO_2 of the iron-wüstite buffer (IW), at any given P and T can be defined as: $\Delta IW = 2\log(X_{FeO}\gamma_{FeO}/X_{Fe}\gamma_{Fe})$; X_{FeO} and X_{Fe} are the mole fractions of FeO in silicate melt and Fe in alloy melt, respectively; γ_{FeO} and γ_{Fe} are the activity coefficients of FeO in silicate melt and Fe in alloy melt, respectively. Calculation of fO_2 using ideal solution model (ideal fO_2) was performed assuming $\gamma_{FeO} = \gamma_{Fe} = 1$; calculation of fO_2 using non-ideal solution model (non-ideal fO_2) performed assuming $\gamma_{FeO} = \sim 1.5$ (Holzheid et al., 1997; O'Neill and Eggins, 2002). Activity coefficients of Fe in Fe-rich melt, γ_{Fe}, were calculated using the ε-approach, which takes into account the non-ideal interaction between all the components in the Fe-rich alloy melt (Ma, 2001; Chi et al., 2014; Wood et al., 2013). The online "Metal Activity Calculator" (http://www.earth.ox.ac.uk/~expet/metalact/) provided by the University of Oxford (Wood et al., 2013) was used to calculate the Fe-activity in alloy melt. The calculated ideal fO_2 values are in general ~0.7 log units lower than the non-ideal fO_2 values. The non-ideal fO_2 for the Knippa–Fe–Ni–S runs were around IW-0.7. The non-ideal fO_2 of the Knippa–Fe–Ni–Si and Knippa–Fe–Ni–S–Si runs ranged from IW-1.3 to IW-4.7, decreasing with decreasing FeO content in silicate melt or increasing Si content in alloy melt. The fO_2 mentioned in the text refers to non-ideal fO_2. n.d: no carbonate was detected by FTIR. √: measured; X: not measured. SM – Silicate melt, AM – Alloy melt, Cpx – Clinopyroxene, SulfM – Sulfide melt, $D^{metal/silicate}$ – C in AM/C in SM. For each sample, 3–6 spots were analyzed by SIMS and 2–5 spots were analyzed by FTIR. Numbers in parentheses are 1σ standard deviation based on replicate analyses; 59(2) should be read as 59 ± 2 and 5.88 (39) should be read as 5.88 ± 0.39.

[a] Ideal fO_2.
[b] Non-ideal fO_2.
[c] Carbon as carbonate.
[d] The water content was measured by FTIR using the Beer–Lambert law at extinction coefficient = 60 and 90 $L\,mol^{-1}\,cm^{-1}$ for water at ~3550 cm^{-1}, respectively.
[e] NBO/T = 2 total O/T − 4 (T = Si + Ti + Al + Cr + P).
[f] Non-hydroxyl hydrogen calculated based on difference between bulk water measured by SIMS and water measured by FTIR using the Beer–Lambert law at extinction coefficient = 60 and 90 $L\,mol^{-1}\,cm^{-1}$ for water at ~3550 cm^{-1}, respectively. See text for details.

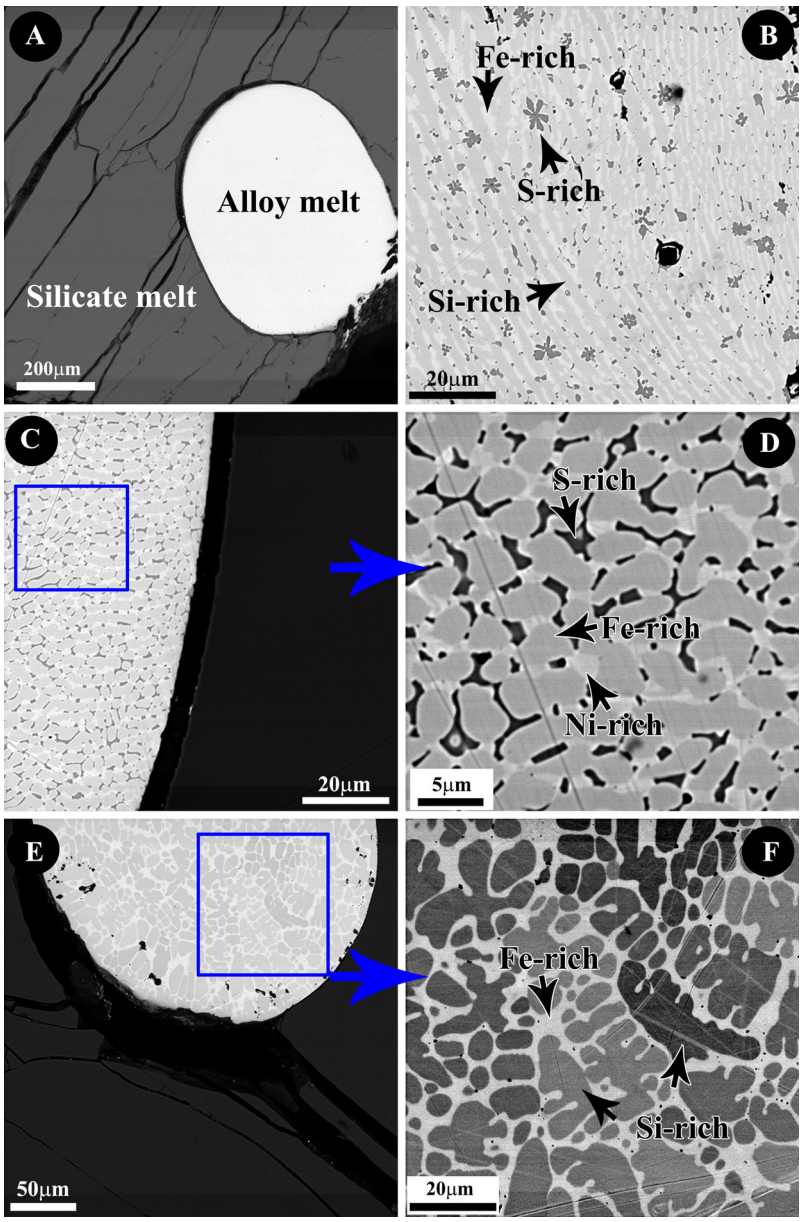

Fig. 1. Selected back-scattered electron images of run products. (A) Coexistence of quenched silicate melt and alloy melt from run G321-07 in the Knippa–Fe–Ni–Si system. (B) Detailed texture of quenched alloy melt from run G330-16 in the Knippa–Fe–Ni–S–Si system. (C) Coexistence of quenched silicate melt and alloy melt from run G316-02 in the Knippa–Fe–Ni–S system. (D) Detailed texture of quenched alloy melt in (C). (E) Coexistence of quenched silicate melt and alloy melt from run G326-12 in the Knippa–Fe–Ni–Si system. (F) Detailed texture of quenched alloy melt in (E).

and prevent leakage of alloy melt, experiments were held at 850 °C for 1–3 h, and then raised to the desired, nominal temperature of the experiment. During the run, temperature was monitored and controlled using a type-C thermocouple. All experiments were brought down ≤100 °C within 10–20 s by switching off the electric power to the heater.

2.3. Analytical procedure

The recovered capsules were sectioned longitudinally into two halves using a wire saw. Both halves were mounted in Crystal Bond® and polished with 0.3 μm aluminum slurry on a lapidary wheel. Each of the samples after polishing was immersed into ~100 ml acetone for at least 24 h to remove completely the Crystal Bond. Cameca SX50 and Cameca SX100 electron microprobes were used for determining the major and minor element compositions of silicate melt and the alloy melt, respectively as well carbon content of alloy melt. A Cameca IMS 1280 ion microprobe was used for determining the bulk carbon and water contents in silicate glasses, and Raman and Fourier transformed infrared (FTIR) spectroscopies were used for determining and quantifying the possible C–H–O species in the silicate glasses following methodologies detailed in recent studies (e.g., Chi et al., 2014; Duncan and Dasgupta, 2014). A complete description of the analytical conditions and instrumental calibration for each of the technique employed is provided in Supplementary Text and Supplementary Figs. 1 and 2.

3. Results

3.1. Texture of the experimental products

All the experiments produced quenched blobs of alloy melt embedded in silicate glasses (Fig. 1). The alloy melt was exsolved into

a few phases during quenching (Fig. 1), but only runs G317-03 and G318-04, which contained about 7 wt% and 10 wt% sulfur in the starting metal mixture, respectively, had two immiscible alloy melt phases during the run (sulfide liquid and S-poor alloy melt). Runs G321-07 and G322-08 also contained a small fraction of residual clinopyroxene at the bottom of the sample capsules.

3.2. Major element composition and estimation of oxygen fugacity

The major element compositions of silicate melt and alloy melt are tabulated in Supplementary Tables 1 and 2, respectively. Compared to the composition of starting silicate, the silicate melt compositions from the Knippa–Fe–Ni–S runs were moderately FeO-rich (15.5–17 wt%), due to oxidation of a small fraction of Fe in the alloy. However, the silicate melts in the Knippa–Fe–Ni–Si and Knippa–Fe–Ni–S–Si runs became SiO_2-rich (45–54 wt%) but depleted in FeO (0.1–9.2 wt%) due to the reduction of FeO in silicate melt by Si in alloy melt via the reaction of 2FeO (silicate) + Si (alloy) = SiO_2 (silicate) + 2Fe (alloy). The values of silicate melt NBO/T are in the range of 0.81 to 1.54 (see Table 2). The Ni content of alloy melt ranged from ~4.5 to 7.2 wt%, and the Fe content of alloy melt ranged from ~82 to 92 wt%. The sulfur content in alloy melt in the Knippa–Fe–Ni–S runs ranged from ~2.0 to 5.0 wt%, while Si content in alloy melt in the Knippa–Fe–Ni–Si and Knippa–Fe–Ni–S–Si runs ranged from <0.1 to ~10 wt%. The sulfur content in sulfide liquid in runs G317-03 and G318-04 was up to ~26 wt%, but the sulfide liquids were not considered further in this study.

Following the method used in many previous studies (e.g., Bouhifd et al., 2013; Dasgupta et al., 2013a; Chi et al., 2014; Boujibar et al., 2014), the oxygen fugacity, fO_2 prevailing during the experiments was calculated from the equilibrium of Fe-rich alloy melt and FeO-bearing silicate melt. Our experiments covered log fO_2 range of IW-0.6 to IW-4.7 (see footnote of Table 2).

3.3. Bulk water content and C–H–O species in silicate melt

The bulk H contents in silicate melt, expressed as H_2O and measured by SIMS, ranged from ~0.07 to 0.68 wt% with most values between ~0.25 and 0.45 wt%. The bulk water content in this study was similar to lower, compared to previous, similar studies (Wetzel et al., 2013; Dasgupta et al., 2013a; Chi et al., 2014; Stanley et al., 2014). The variation of water content in our silicate melt allowed us to investigate its effect on carbon solubility in silicate melt and partitioning between alloy melt and silicate melt at a fixed temperature and pressure, and also fO_2 in the runs in the Knippa–Fe–Ni–S system (see below).

Raman spectra were collected from the silicate glasses of all the runs and typical spectra are shown in Fig. 2A. The recognition of C–H–O species from Raman spectra was affected by fluorescence in all the silicate glasses. However, it remains clear that peaks at ~4100 and 2900 cm^{-1} from glasses synthesized at reduced conditions in the Knippa–Fe–Ni–S–Si and Knippa–Fe–Ni–Si systems are owing to the presence of molecular hydrogen (H_2) and methane (CH_4), respectively. Whereas the asymmetrical broad band between 3350 and 3650 cm^{-1} is associated with OH^- ions and molecular water (Mysen et al., 2009; Dasgupta et al., 2013a; Chi et al., 2014). The iron-carbonyl peak as has been observed by Wetzel et al. (2013) was not observed in our Raman spectra, although our silicate melt (runs in the Knippa–Fe–Ni–S system) had FeO* content up to 17 wt%. The absence of any features that can be associated with Fe-carbonyl or other Fe–C species suggests that FeO* content of our experimental melts couldn't possibly have any causal relationship with C solubility.

FTIR spectra were obtained for all the glasses except for runs G315-01 and G322-08, and selected spectra are shown in Fig. 2B. The samples synthesized at relatively oxidized conditions in the Knippa–Fe–Ni–S system showed carbonate doublets at 1420 and 1510 cm^{-1}, which are absent for the samples synthesized at relatively reduced conditions in the Knippa–Fe–Ni–Si and Knippa–Fe–Ni–S–Si systems. All the spectra had a broad peak at ~3550 cm^{-1}, indicating the presence of OH^- in the glasses. The dissolved OH^- content and carbonate content were quantified using the Beer–Lambert law. The extinction coefficient ($\varepsilon = 375$ L mol^{-1} cm^{-1}) used in Chi et al. (2014) for a similar melt composition was used for quantifying the carbonate content, and ε of 60–90 L mol^{-1} cm^{-1} for water at ~3550 cm^{-1} were used for quantifying the H_2O content. The reason for choosing ε of 60 and 90 L mol^{-1} cm^{-1} as two bounds is that these values cover the main range reported for extinction coefficient of water at ~3550 cm^{-1} in basaltic to rhyolitic melts (e.g., Stolper, 1982). We note, however, that no correlation has been observed for reported ε for OH^- as a function of melt composition, which justifies our choice of using two fixed values of ε for different experimental glass compositions generated in our study rather than using different ε for different experiments. The results showed that OH^- (expressed as H_2O)

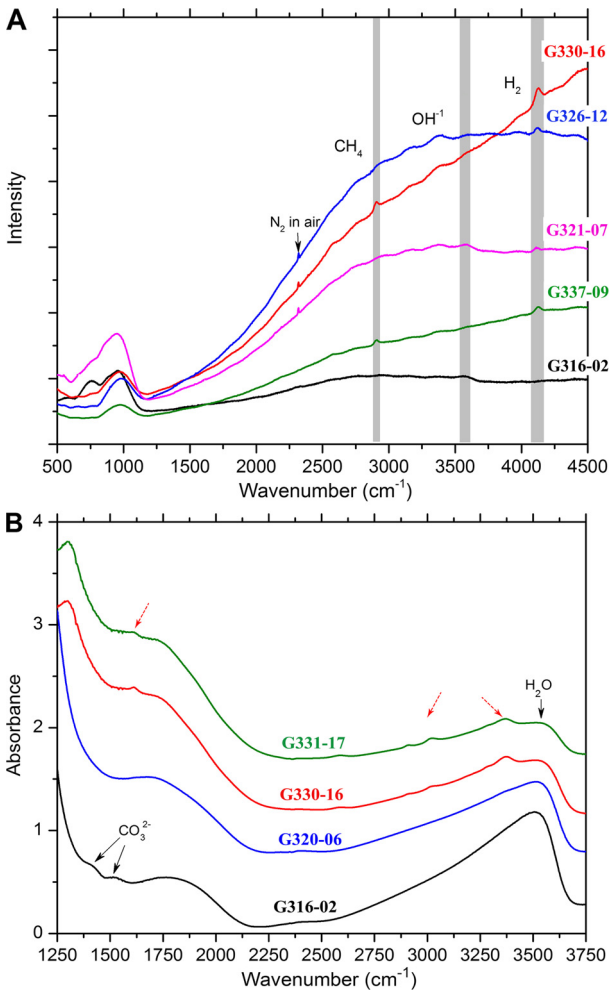

Fig. 2. Representative Raman (A) and FTIR (B) spectra of experimental silicate glasses from this study showing regions associated with C–H–O volatile species. See Table 2 for experimental conditions corresponding to these experiments. The peaks indicated by dashed arrows in panel (B) remain unspecified, but they might be due to the stretching vibration of N–H (Busigny et al., 2003; Stanley et al., 2014) or organic contamination on the sample surface (e.g., fingerprints). Because these peaks are observed in the most reduced samples (log fO_2 < IW-4), it is highly likely they are due to N–H stretching vibration, but contamination cannot be ruled out for the two peaks at ~3000 cm^{-1}. The sample thicknesses for FTIR measurement are 300 μm for G316-02, 340 μm for G320-06, 370 μm for G330-16, and 360 μm for G331-17.

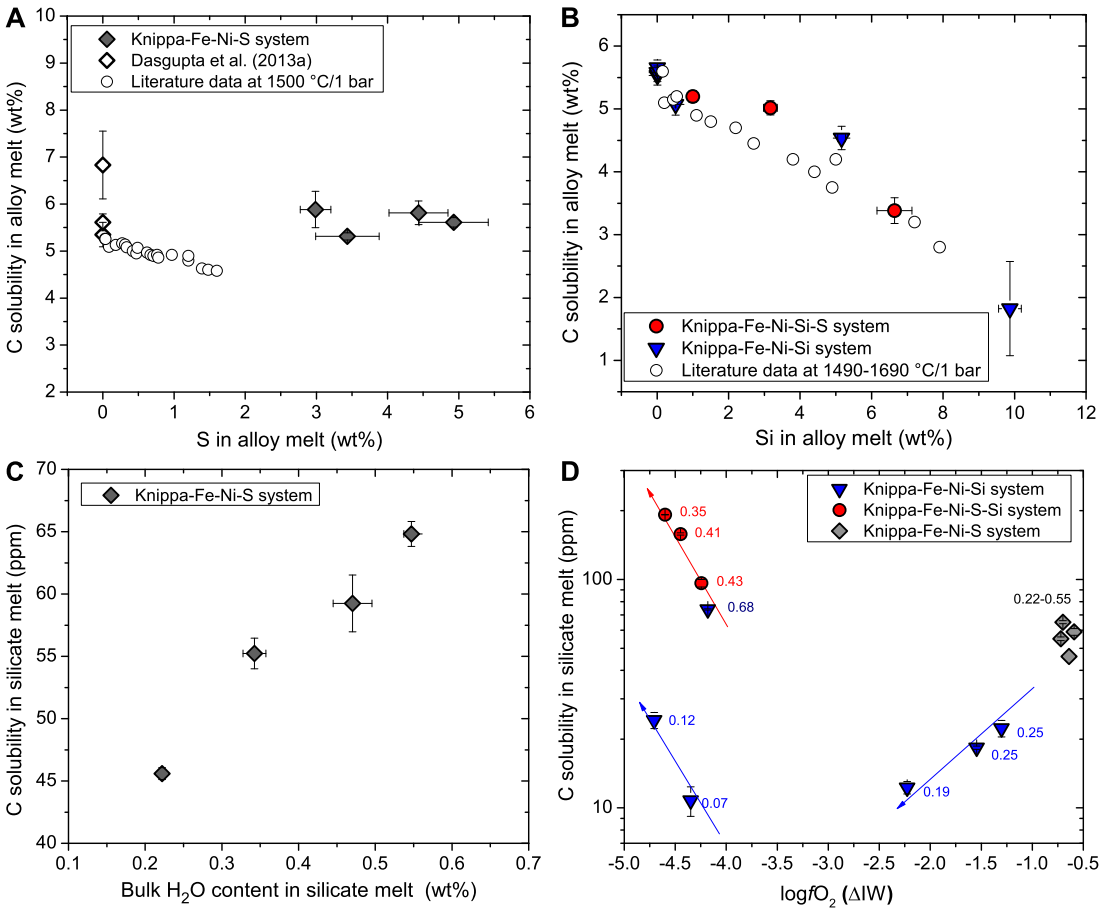

Fig. 3. Carbon solubility in alloy melt as a function of S content in alloy melt (A) and Si content in alloy melt (B), and carbon solubility in silicate melt as a function of water content in silicate melt (C) and oxygen fugacity (D). The labeled numbers are bulk water contents in silicate melt in wt%. The data of unfilled diamonds in panel (A) are from 3 GPa, 1600 °C experiments of Dasgupta et al. (2013a), and the literature data (unfilled circles) in panels (A) and (B) are from Bouchard and Bale (1995) and the references therein. Note that unlike 1 bar experiments, carbon solubility in the Fe-rich alloy melt at 3 GPa (this study) does not decrease with increasing sulfur content from 0 to ~5 wt%.

contents in the silicate glasses ranged from ~0.02 to 0.34 wt%, significantly lower than the bulk H_2O contents determined by SIMS (Table 2), in particular at reduced conditions.

Assuming that the other water is mainly in the form of molecular hydrogen (H_2), the calculated H_2 contents in silicate melt were between 0.0017 wt% and 0.0383 wt% (Table 2). We point out that H_2 content estimated this way provides an upper bound as clearly a small fraction of the hydrogen not present as OH^- or H_2O is present as CH_4 and other ions or molecules bonded to carbon and may be even nitrogen, and molecular H_2 mentioned hereafter refers to all non-hydroxyl hydrogen in silicate melt. The calculated carbon contents in the form of carbonate for the runs in the Knippa–Fe–Ni–S system were ~10 ppm, consistent with the result of 7 ppm of run B70 performed at similar conditions by Chi et al. (2014).

3.4. Carbon contents in Fe-rich alloy melt and silicate melt at graphite-saturation

Carbon solubilities in alloy melt and silicate melt at graphite-saturation are tabulated in both Table 2 and Supplementary Table 2. The C-solubility in alloy melt in the Knippa–Fe–Ni–S system is ~5.6 wt% and appears not to be affected by the presence of sulfur in alloy melt (Fig. 3A). However, the C-solubility in alloy melt in the Knippa–Fe–Ni–Si and Knippa–Fe–Ni–S–Si systems decreases from ~5.6 wt% to ~1.8 wt% with Si content in alloy melt increasing from <0.1 to ~10 wt% (Fig. 3B).

C-solubility in silicate melt ranges from ~10 to ~190 ppm. It is ~45–65 ppm in the Knippa–Fe–Ni–S system, increasing with increasing water content (Fig. 3C). The C-solubility in silicate melt in the Knippa–Fe–Ni–Si and Knippa–Fe–Ni–S–Si systems depends not only on water content in silicate melt but also on fO_2 (Fig. 3D). For the runs with ~0.35–0.42 wt% H_2O in the Knippa–Fe–Ni–S–Si system, the carbon content in silicate melt increases from ~96 to 192 ppm with fO_2 decreasing from IW-4.2 to IW-4.6. The C-solubility in silicate melt in the Knippa–Fe–Ni–Si system is generally lower (~10–25 ppm) and decreases with decreasing fO_2 from IW-1.4 to IW-2.2 and decreasing water content from ~0.25 to 0.19 wt%. However, C-solubility trend reverses and increases with decreasing fO_2 from ~IW-4.3 to IW-4.7 and increasing water content from ~0.07 to 0.12 wt%, as in the case of the C-solubility in silicate melt in the Knippa–Fe–Ni–S–Si system. One sample (run G322-08) with 0.68 wt% H_2O and fO_2 of IW-4.2 in the Knippa–Fe–Ni–Si system contained ~74 ppm carbon, which appears to be consistent with the solubility values in the Knippa–Fe–Ni–S–Si system.

Using the model of Holloway et al. (1992), the calculated carbon contents in the form of carbonate were ~2 ppm for the runs in the Knippa–Fe–Ni–S system, whereas for the runs in the Knippa–Fe–Ni–Si and Knippa–Fe–Ni–S–Si systems, they were below 0.5 ppm, indicating negligible carbon as carbonate in reduced silicate melt. Meanwhile, regardless of fO_2 or bulk water content in the runs, a strong, positive correlation was observed between the non-carbonate carbon and molecular H_2 in silicate melt (Fig. 5A). These together with the Raman methane peak (Fig. 2A)

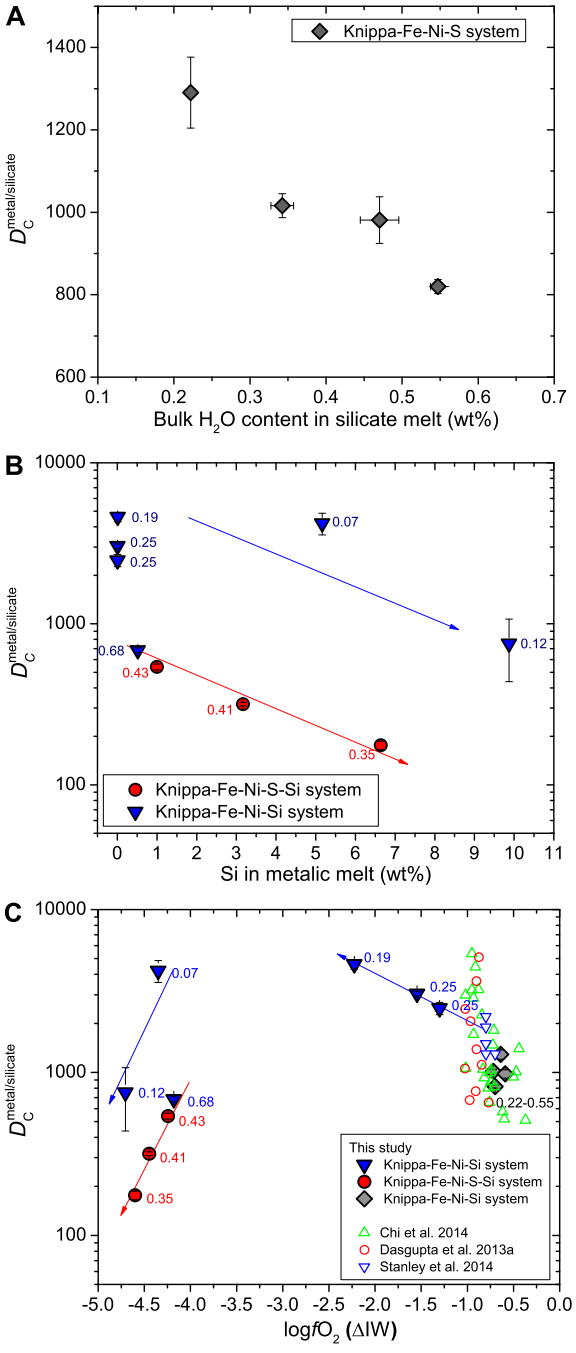

Fig. 4. Partition coefficient of carbon between metallic alloy melt and silicate melt ($D_C^{metal/silicate}$) as a function of water content in silicate melt (A), Si content in metallic alloy melt (B), and oxygen fugacity (C). The labeled numbers are bulk water content in silicate melt in wt%. Also plotted for comparison in (C) are previously determined experimental $D_C^{metal/silicate}$ values from Dasgupta et al. (2013a), Chi et al. (2014), and Stanley et al. (2014) generated over 1–5 GPa, 1350–2000 °C, and bulk silicate melt water content of 0.19–2.06 wt%.

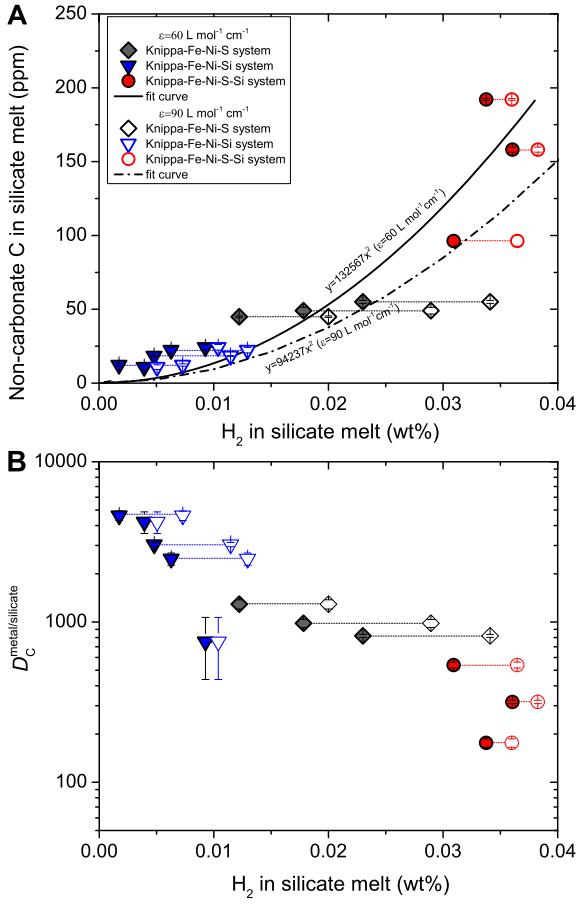

Fig. 5. The correlations between molecular H_2 in silicate melt and non-carbonate carbon in silicate melt (A), and $D_C^{metal/silicate}$ (B) from our 3 GPa, 1600 °C experiments. The strong positive correlation in panel (A) indicates that the carbon species in silicate melt is mostly as hydrogenated carbon (methane). The negative correlation in panel (B) indicates the strong controlling effect of molecular hydrogen in silicate melt or fH_2 on carbon partitioning between alloy melt and silicate melt. The data in panel (A) are fitted as $y = 132\,567x^2$ (solid curve) and $y = 94\,237x^2$ (dashed curve) where x and y refer to H_2 (wt%) and non-carbonate carbon (ppm), respectively, which combined with Eq. (8) can be used to calculate methane content in silicate melt as a function of oxygen fugacity and melt bulk water content (see text). Note that molecular H_2 here refers to all the non-hydroxyl hydrogen in silicate melt and equals the bulk hydrogen determined by SIMS minus the hydroxyl hydrogen determined by FTIR using the Beer–Lambert law (at $\varepsilon_{OH^-} = 60$ and 90 L mol^{-1} cm^{-1} for closed and open symbols, respectively). Non-carbonate carbon and bulk carbon measured using SIMS are the same for all experiments with log fO_2 < IW-1.3. In both panels, the estimates of molecular H_2 in silicate glass from the same experiment are connected by thin dashed line where the two estimates derive from different estimates of the concentration of dissolved H_2O using different extinction coefficients. The form of the fit chosen in (A) is guided by the assumption that essentially all non-carbonate carbon dissolved in our glasses are in the form of CH_4 and solubility of CH_4 must be proportional to the square of hydrogen fugacity, fH_2 and H_2 solubility in melt is directly proportional to fH_2.

imply that carbon species in silicate melt of the present study is mostly as methane.

3.5. Partition coefficient of carbon between alloy melt and silicate melt

$D_C^{metal/silicate}$ was calculated based on the measured carbon contents in alloy melt and silicate melt. The $D_C^{meal/silicate}$ values in this study varied from 180 to 4600 (Table 2; Fig. 4). The $D_C^{metal/silicate}$ values in the Knippa–Fe–Ni–S system decrease from 1300 to 800 with increasing H_2O content in silicate melt (Fig. 4A). The $D_C^{metal/silicate}$ values in the Knippa–Fe–Ni–Si and Knippa–Fe–Ni–S–Si systems decrease from 4600 to 180 with increasing Si content in alloy melt (Fig. 4B). Decreasing fO_2 appears to first increase the $D_C^{metal/silicate}$ value and then decrease the $D_C^{metal/silicate}$ value (Fig. 4C). It should be noted that fO_2 is negatively correlated with the Si content in alloy melt, therefore the effect of Si in alloy melt and the effect of fO_2 on carbon partitioning are coupled. The water effect on $D_C^{metal/silicate}$ can also be seen from Fig. 4B and 4C at a given Si content in alloy melt or fO_2, i.e., increasing water content causes a decrease in $D_C^{metal/silicate}$. Fig. 5B shows that regardless of fO_2 or bulk water content, $D_C^{metal/silicate}$ value is neg-

atively correlated with non-hydroxyl hydrogen content in silicate melt, indicating the strong controlling effect of fH_2 in silicate melt on carbon partitioning.

4. Discussion

4.1. Effects of fO_2 and water on carbon dissolution in silicate melt

How the dissolution mechanism of carbon in silicate melt changes is the key to understand the effects of water and fO_2 (Fig. 3), and the effects of melt NBO/T, temperature, and pressure (Dasgupta et al., 2013a; Chi et al., 2014), on carbon solubility in silicate melt. Although previous spectroscopic studies have shown that the carbon species in mafic silicate melt at fO_2 of around FMQ ± 2 are dominated by carbonate, the carbon speciation in reduced mafic melt with fO_2 below the IW buffer remains unclear and more variable (Holloway et al., 1992; Kadik et al., 2004; Mysen et al., 2009, 2011; Ardia et al., 2013; Dasgupta et al., 2013a; Wetzel et al., 2013; Stanley et al., 2011, 2014; Chi et al., 2014). Kadik et al. (2004) suggested that carbon is mainly dissolved as atomic carbon or amorphous carbon in their silicate melt with 1–2 wt% H_2O and fO_2 of ~IW-2.3, and that Si–C complex might exist in their silicate melt. Conversely, Mysen et al. (2009, 2011) found strong Raman peaks assigned to methane and other hydrogenated carbon species rather than Si–C complex in SiO_2–Na_2O melt with ~1 wt% water and fH_2 buffered by the IW buffer. Wetzel et al. (2013) showed the presence of iron carbonyl [$Fe(CO)_5$] besides methane in silicate melt with around 0.5 wt% water and fO_2 below IW-0.5. However, Dasgupta et al. (2013a) and Chi et al. (2014) showed coexisting carbonate and methane and probably other hydrogenated carbon species but no iron carbonyl in silicate melt with ~0.4–2.0 wt% water and fO_2 below IW-0.4. Stanley et al. (2014) showed that their silicate melt with ~0.4 wt% water does not contain hydrogenated carbon but probably carbonyl or other C=O bearing species at fO_2 between IW-0.3 and IW-0.8. For our runs in the Knippa–Fe–Ni–S system, Raman and FTIR spectra show that only a small fraction of carbon is dissolved in the silicate melt as carbonate, and no Raman or FTIR peaks can be assigned to iron carbonyl or Si–C complex. For our runs in the Knippa–Fe–Ni–Si and Knippa–Fe–Ni–S–Si systems, methane is the only observed carbon species in silicate melt. These together with the strong correlation between non-carbonate carbon and molecular H_2 (Fig. 5A) indicate that in our silicate melt methane is the dominant carbon species.

At a given P–T and melt composition, the effects of H_2O and fO_2 on carbon dissolution in silicate melt at graphite-saturation can be better understood with the following reactions:

$$H_2O^{vapor} = H_2^{vapor} + 1/2O_2^{vapor} \quad (1)$$

$$C^{graphite} + O_2^{vapor} = CO_2^{vapor} \quad (2)$$

$$CO_2^{vapor} + O^{2-\,melt} = CO_3^{2-\,melt} \quad (3)$$

$$C^{graphite} + 2H_2^{vapor} = CH_4^{melt} \quad (4)$$

$$xC^{graphite} + y/2H_2^{vapor} = C_xH_y^{melt}\ (\text{methyl or alkyne group}) \quad (5)$$

According to these reactions, the dissolution of carbonate, methane, and/or methyl groups in silicate melt must be controlled by the fugacities of H_2O, H_2, and O_2 at graphite-saturation. For example, increasing fH_2 must increase the dissolution of carbon as methane in silicate melt according to reaction (4). In the experiments where fO_2 is buffered by the coexisting metallic alloy melt and silicate melt, fH_2 must increase with increasing the bulk H_2O content according to reaction (1), leading to more carbon dissolved as methane or methyl groups in silicate melt according to reactions (4) and (5).

Our experiments in the Knippa–Fe–Ni–S system have nearly identical fO_2 and carbon contents in the form of carbonate (see Table 2). The observed positive correlation between the bulk water content and the carbon solubility in silicate melt (Fig. 3C) can thus be interpreted as resulting from increasing carbon dissolution as methane with increasing bulk water content in silicate melt according to reactions (1) and (4). For experiments in the Knippa–Fe–Ni–Si system, the decrease in carbon solubility with decreasing fO_2 from IW-1.3 to IW-2.2 (Fig. 3D) on one hand is because of the decreased carbonate dissolution with decreasing fO_2, on the other hand is because of the lower bulk water content, which results in decreased fH_2. The increase of carbon solubility with decreasing fO_2 from IW-4.2 to IW-4.7 in the Knippa–Fe–Ni–Si and Knippa–Fe–Ni–S–Si systems (Fig. 3D) is owning to increased fH_2 and thus enhanced solubility of methane in silicate melt with decreasing fO_2 and increasing bulk water content (Table 2 and Fig. 5A). According to this study and Hirschmann et al. (2012), molecular H_2 may be dominant over OH^- and/or H_2O in hydrous silicate melt at $\log fO_2 <$ IW. We thus believe that previous experiments with ~0.5 wt% bulk water and fO_2 below the IW buffer may indeed contain a certain amount of methane, although it was not detected by Raman spectroscopy.

Chi et al. (2014) showed that silicate melt composition may considerably affect the solubility of carbon in silicate melt at IW-1 $< \log fO_2 <$ IW. Because carbon solubility in more reduced silicate melt ($\log fO_2 <$ IW-1) is significantly affected by water, the samples with similarly low water contents (0.07–0.25 wt% H_2O) but different NBO/T values were chosen in order to assess the effect of silicate melt major element composition on carbon solubility in the present reduced silicate melt (runs G319-05, G320-06, G321-07, G326-12, and G329-15). This evaluation shows that carbon solubility range of only ~11 ppm exists in these samples with NBO/T ranging from 0.81 to 1.22, which is at least an order of magnitude smaller than the entire range of carbon solubility observed in our glasses. This indicates that the effect of silicate melt major element composition is indeed small compared to the effect of water (see Fig. 5A).

4.2. Factors controlling $D_C^{metal/silicate}$ and parameterization

The factors controlling carbon dissolution in silicate melt and in alloy melt must control $D_C^{metal/silicate}$. It has been shown that 0–5 wt% sulfur in alloy melt does not have considerable effect on carbon solubility, whereas increasing Si decreases the carbon solubility. Therefore, the variation of $D_C^{metal/silicate}$ in the Knippa–Fe–Ni–S experiments (Fig. 4A) is simply due to the variation of carbon solubility in silicate melt caused by the variation of bulk water content, whereas for the Knippa–Fe–Ni–Si and Knippa–Fe–Ni–S–Si experiments, the $D_C^{metal/silicate}$ variation is a result of combined variation of fO_2, bulk water content, and silicon content in alloy melt (Fig. 4B and 4C).

The compiled values of $D_C^{metal/silicate}$ from our study and those from literature are plotted in Fig. 4C and in Supplementary Fig. 3. Due to the limited range of carbon solubility in alloy melt (1.82 to 5.88 wt% in this study; 4.5–7.0 wt% in Dasgupta et al., 2013a; 4.4–7.4 wt% in Chi et al., 2014; 6.7–8.3 wt% in Stanley et al., 2014), $D_C^{metal/silicate}$ varies mainly as the variation of carbon content in silicate melt, and our $D_C^{metal/silicate}$ data obtained at a single P–T condition cover the previous $D_C^{metal/silicate}$ data range (Fig. 4C and Supplementary Fig. 3), indicating again the strong effects of fO_2 and the bulk water content or the strong effect of fH_2 on carbon partitioning (Fig. 5B). Fig. 4C shows that $D_C^{metal/silicate}$ tends to increase first with decreasing fO_2 but then decrease with furthering decrease in fO_2. The discrete change of $D_C^{metal/silicate}$ is owing to

the change of fO_2 and bulk water content dependent change in carbon speciation and solubility in silicate melt, and other parameters as has been discussed above. Using the $D_C^{metal/silicate}$ compiled in Fig. 4C, two empirical parameterizations were derived.

At IW-1.3 < log fO_2 < IW:

$$\log D_C^{metal/silicate} = 2100/T + 260P/T - 0.67NBO/T - 0.32\Delta\text{IW} - 1.65X_{H_2O}^{silicate} - 11.5X_{Ni}^{metal} + 2.86 \quad (R^2 = 0.83) \quad (6)$$

At log fO_2 < IW-1.3 and 3 GPa, 1600 °C:

$$\log D_C^{metal/silicate} = -0.33NBO/T + 0.045\Delta\text{IW} - 113X_{H_2O}^{silicate} - 5.3X_{Ni}^{metal} - 5.03X_{Si}^{metal} + 5.03 \quad (R^2 = 0.97) \quad (7)$$

T is in K, and P is in GPa, and X refers to mole fraction. Eq. (6) uses 41 experiments with data from this study and from Dasgupta et al. (2013a), Chi et al. (2014), Stanley et al. (2014) covering P of 1–5 GPa and T of 1350–2100 °C, whereas Eq. (7) uses data only from this study. The main difference between Eq. (6) and the parameterization of Chi et al. (2014) is that the present parameterization includes the term for effect of water in silicate melt and expresses fO_2 in ΔIW scale besides adding four more data points from the present study. The reason for deriving two parameterizations is that at IW-1.3 < log fO_2 < IW carbonate continues to be a significant C species in silicate melt, while at log fO_2 < IW-1.3 and modest level of hydration methane appears to be the main C-bearing species in silicate melt.

4.3. Core/mantle partitioning of carbon in MO

Recent studies suggested that planetary core-formation may have occurred as a largely continuous process with core segregation starting well before the end of Earth's accretion, rather than a single event at fixed P–T–fO_2 conditions (e.g., Wade and Wood, 2005; Wood et al., 2006, 2008; Rubie et al., 2011). To satisfy the abundance patterns of mild to moderately siderophile elements in silicate mantle, these authors invoked early accretion of highly reduced materials, followed by gradually oxidized materials. The corresponding log fO_2 in the MO may have been as low as ~IW-5 but gradually increased to ~IW-2 (e.g., Rubie et al., 2011). At reduced conditions, silicon is likely to be the most abundant light elements entering the alloy melt (Wood et al., 2008; Ricolleau et al., 2011; Tsuno et al., 2013; Siebert et al., 2013). The silicon content in our alloy melt is up to 10 wt%, which is at the high end of the estimated, likely silicon in the core-forming alloy melt (Allegre et al., 1995; Ricolleau et al., 2011; Rubie et al., 2011; Siebert et al., 2013). As noted above (see also Fig. 5), hydrogen is important in affecting the dissolution and partitioning of carbon, but its concentration in MO remains largely unknown. Based on the solubility of hydrogen in an MO overlain by a thick steam atmosphere, Hirschmann (2012) and Ardia et al. (2013) proposed that MO hydrogen content ≤1000 ppm is possible. The estimated water (H_2O) content of the bulk Earth by Marty (2012) is between 0.1 and 0.3 wt%. If one assumes that this amount of water was present in Earth's MO, H_2O content ≤0.3 wt% (≤330 ppm H) may have been possible due to negligible partitioning of H to the core.

Chi et al. (2014) used their parameterization to predict carbon partitioning between planetary core and mantle at P–T–fO_2 conditions corresponding to the base of the MOs. The results showed that core-formation of both Earth and Mars may have resulted in the entire carbon segregated into the core, but carbon in the lunar mantle could possibly be set up by equilibrium core–mantle

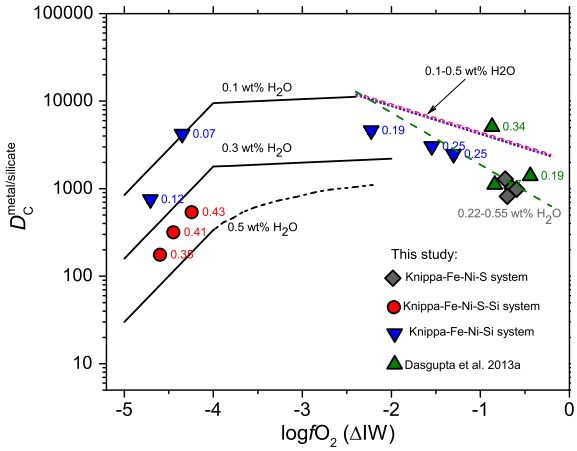

Fig. 6. The experimentally measured $D_C^{metal/silicate}$ from 3 GPa, 1600 °C as a function of estimated fO_2 and bulk water content of silicate melt compared with the existing parameterization that predict the dependence of $D_C^{metal/silicate}$ on fO_2 and silicate melt water content. The experimental data are from this study and those from Dasgupta et al. (2013a). The plot shows that the calculated $D_C^{metal/silicate}$ values using Eq. (6) (short dashed lines) do not depend considerably on bulk water content in silicate melt but increase markedly with decreasing oxygen fugacity. However, the $D_C^{metal/silicate}$ values calculated using Eq. (7) (black solid lines) show a significant dependence on bulk water content in addition to fO_2. Also plotted for comparison using the long dashed line is the parameterization of Chi et al. (2014). The fit using Eq. (6) and that from Chi et al. (2014) are plotted only down to log fO_2 ~ IW-2.5 as these fits were derived based on relatively oxidized experiments (see text; Chi et al., 2014), whereas the fit using Eq. (7) is chiefly plotted between IW-5 and ~IW-2. The parameters in Eqs. (6) and (7) are fixed at $X_{Ni}^{metal} = 0.04$, NBO/T = 0.9, values similar to average values in our experiments. Si content in alloy melt is varied from 10 to 0.1 wt% at log fO_2 from IW-5 to IW-4 according to present study. The labeled numbers are bulk water contents in silicate melt in wt%. The black dashed line refers to possible trend of $D_C^{metal/silicate}$ with varying fO_2 and melt water content at conditions where our parameterizations do not have good data coverage.

fractionation in an MO. However, limited by their dataset, Chi et al. (2014) did not consider the effects of varying log fO_2 below ~IW-1.5 and water in silicate melt on carbon partitioning. The above parameterizations (Eqs. (6) and (7)) allow us to predict the variation of $D_C^{metal/silicate}$ as the variations of fO_2 and water at 3 GPa and 1600 °C (Fig. 6). Fig. 6 shows that increasing water content in silicate melt significantly lowers $D_C^{metal/silicate}$ value calculated based on Eq. (7). The extrapolation of Eq. (6) and the parameterization of Chi et al. (2014) to log fO_2 < IW-2 leads artificially to exceedingly high $D_C^{metal/silicate}$ values. Therefore, if the log fO_2 in MO had evolved from IW-5 to IW-2, and if water content was as high as 0.9 wt% (1000 ppm H), the $D_C^{metal/silicate}$ value may likely be between 10 and 100 at low fO_2 (Fig. 6). The increase of $D_C^{metal/silicate}$ with increasing log fO_2 from IW-5 to IW-2 may also imply that there may have been less carbon segregated into the core during the early accretion of highly reduced material. However, if the MOs were relatively dry with less than 0.1 wt% H_2O, regardless of fO_2, carbon should have effectively been segregated into the core because of the exceedingly high $D_C^{metal/silicate}$. Furthermore, it should be noted that the present study was performed at a single P–T condition. Silicon solubility in alloy melt may vary with P–T and fO_2 (Ricolleau et al., 2011; Tsuno et al., 2013; Siebert et al., 2013), and the molecular H_2 content in silicate melt at a given bulk water content and fO_2 may also vary with varying pressure and temperature (Hirschmann et al., 2012). All these could affect $D_C^{metal/silicate}$. Hence to better understand the fractionation of carbon in MO, high P–T experiments with various fO_2 and water contents are required.

One final consideration is the availability of carbon in terrestrial MO and its relation to the fO_2 evolution of the MO. If carbon (along with sulfur) was not present in the early, reduced stage of

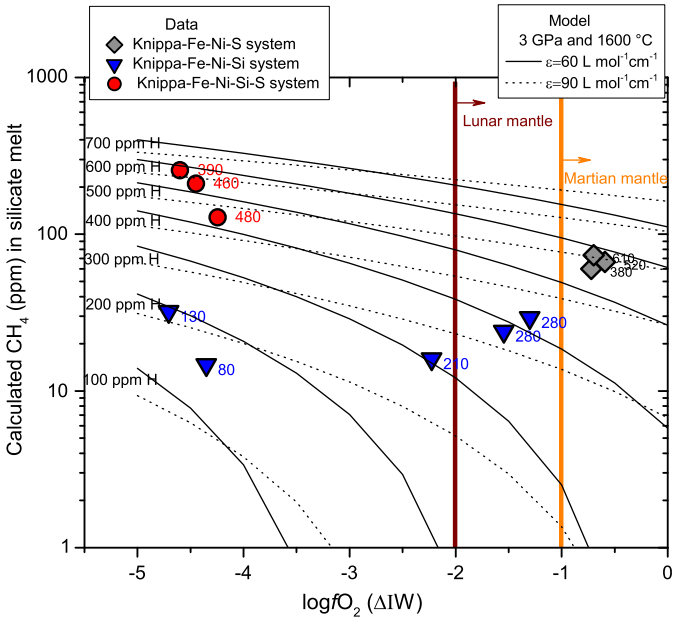

Fig. 7. The calculated methane (CH_4) contents in silicate melt (solid and dotted curves) at 3 GPa and 1600 °C as a function of oxygen fugacity and bulk water (H) content in silicate melt, using Eq. (8) and the correlation shown in Fig. 5A. The solid and dotted curves represent model calculations where molecular H_2 was determined using $\varepsilon_{OH^-} = 60$ and 90 L mol^{-1} cm^{-1}, respectively. The plotted data show the measured abundance of non-carbonate carbon in our experimental silicate melt (Table 2), assumed to be present entirely as methane; the labeled numbers are bulk water (H) contents in silicate melt in ppm. The two vertical lines indicate the lowest oxygen fugacity estimated for lunar mantle and Martian mantle. Our experimental data and model predict the amount of degassed methane from Martian and lunar mantle for a given fO_2 and bulk 'water' content of planetary basalts saturated with graphite.

MO and was delivered at a late stage (after 90%) of accretion when the terrestrial MO already had evolved to less reduced conditions (~IW-2; Wade and Wood, 2005; Wood et al., 2013) then Si in alloy melt and solution of CH_4 in MO might not have influenced $D_C^{metal/silicate}$. If this was the case, then despite the possibility of achieving a $D_C^{metal/silicate} < 100$ in the presence of Si in alloy in a hydrous MO, the $D_C^{metal/silicate}$ values for terrestrial core formation would be those >1000 and effectively all the available carbon would partition to the core of the Earth.

4.4. Carbon degassing from MO and its influence on early planetary atmospheres

The formation of planetary atmosphere may have been coupled with the solidification of planetary MO (e.g., Elkins-Tanton, 2008, 2012). The presence and nature of an atmosphere overlying an MO in turn could significantly influence the thermal evolution of an MO (e.g., Lebrun et al., 2013). However, the redox state of planetary early atmosphere overlying an MO remains unknown (e.g., Hirschmann, 2012; Dasgupta, 2013; Li and Keppler, 2014), in part because the carbon species in the shallow MO have not been constrained.

This study has shown that in modestly hydrated reduced silicate melt with fO_2 ranging from IW-5 to IW-1, carbon is mainly in the form of CH_4, and the carbon content as carbonate is negligible. Thus, carbon in an MO with log fO_2 below IW-2 may have been mostly as CH_4 and degassing of an MO may have only released CH_4 into the overlying atmosphere, even if the bulk water content in the MO was as low as 0.1–0.3 wt%. The most efficient degassing of an MO may have occurred when it experienced significant solidification and volatile enrichment. A post-differentiation planetary MO may not have been saturated with elemental carbon, in part because a significant amount of carbon may have been segregated into the core and in part because water (in particular molecular H_2) in the post-differentiation MO may have accumulated to an elevated content such that the carbon solubility in silicate melt is significantly enhanced in the form of CH_4. The solubility of carbon in silicate mantle minerals is exceedingly low (Shcheka et al., 2006), so that the residual carbon from core-segregation may have been mainly concentrated in the residual silicate melt in the form of CH_4 after significant solidification of an MO, together with reduced species such as ammonia and molecular H_2 (Hirschmann et al., 2012; Bali et al., 2013; Li and Keppler, 2014). Therefore, degassing of such reservoirs enriched in reduced species may have created a reduced early atmosphere consisting mainly of CH_4, molecular H_2, and ammonia. Thus our study suggests that formation of reduced planetary atmospheres rich in CH_4 might have occurred for the proto Earth not only as a transient state soon after collision with reduced impactors (Zahnle et al., 2010; Genda and Abe, 2003) but also at a late stage of crystallization of a reduced and hydrated MO.

4.5. Degassing of C–O–H volatiles via partial melting of reduced planetary mantles

Degassing of reduced carbon species from planetary interior to atmosphere may have potentially maintained the planetary surface temperature above the freezing point of water in early planetary history (e.g., Sagan and Mullen, 1972; Ardia et al., 2013; Wetzel et al., 2013). However, it is poorly understood whether degassing of the reduced planetary mantles at post-MO stage such as for the Martian mantle could have released sufficient dose of reduced C–O–H fluids to explain the early episodes of warm Martian climate (Stanley et al., 2011, 2014; Ardia et al., 2013) or whether warm ancient Martian atmosphere was achieved through other degassed volatiles (e.g., Halevy et al., 2007; Righter et al., 2009; Ding et al., 2014, 2015). Because our experimental condition and generated melt compositions at log fO_2 of ~IW to IW-2 are closely applicable for mantle melting in reduced rocky planets such as Mars (e.g., Musselwhite et al., 2006; Filiberto et al., 2010; Filiberto and Dasgupta, 2011, 2015), our measured concentrations of C–O–H volatiles in equilibrium with graphite are directly relevant for evolution of magmatic volatiles in such planetary bodies.

It is widely argued that the log fO_2 of primary Martian basalts is down to IW-1 and therefore carbon is present in the Martian mantle as graphite/diamond (e.g., Herd et al., 2002; Karner et al., 2007; Wadhwa, 2008; Righter et al., 2008). However, the water content of Martian basalts is subject to considerable controversy, with arguments for both quite dry and hydrous primary magmas with hydrogen content up to 3000 ppm but as low as a few ppm (e.g., Filiberto and Treiman, 2009; McCubbin et al., 2010a, 2010b, 2012; Gaillard et al., 2012). To be able to predict CH_4 content in silicate melt using the correlation in Fig. 5A, an equation was first derived based on our data in Table 2 for calculating molecular H_2 content in silicate melt at given fO_2 and bulk water content:

$$H_2(\text{wt\%}) = aH_2O(\text{wt\%}) - b\Delta\text{IW} - c \quad (8)$$

where $a = 0.0828$–0.0917, $b = 0.0052$–0.0036, and $c = 0.0232$–0.0163, and $R^2 = 0.95$–0.97 for ε of H_2O varying from 60 to 90 L mol^{-1} cm^{-1}.

Using Eq. (8), the calculated CH_4 content in silicate melt at graphite-saturation and at log fO_2 = IW-1 is 3–13 ppm when H = 300 ppm, 50–80 ppm when H = 500 ppm, and 150–190 ppm when H = 700 ppm (Fig. 7). The increase of fO_2 by one log unit would decrease the amount of CH_4 dissolved in silicate melt by

less than 50% when H $\geq$ 500 ppm. These results indicate that a considerable amount of CH_4 may have been in the Martian basalt as long as the estimated water (H) content is applicable to Martian mantle and Martian basalts. Due to the low solubility of carbonate in silicate melt (<10 ppm at 3 GPa, 1600 °C and $\log f O_2$ = IW-1), Stanley et al. (2011) concluded that the degassing of CO_2 to the Martian atmosphere may be insufficient to create greenhouse conditions required by possible presence of liquid water on Martian surface. Our study suggests that degassing of Martian mantle may have released considerable CH_4 to help maintain Martian surface temperature above the freezing point of water. This is in contrast to previous studies (Stanley et al., 2014) that suggested negligible CH_4 released from the Martian mantle into atmosphere.

The $\log f O_2$ of lunar mantle is between IW-2 and IW (e.g., Wadhwa, 2008; Nicholis and Rutherford, 2009). Wetzel et al. (2013) proposed that degassing of lunar mantle may release reduced carbon species such as CH_4 and CO into the atmosphere. However, whether degassing of lunar mantle released CH_4 into the early atmosphere depends not only on $f O_2$ but also on the bulk water content in silicate melt. The estimated hydrogen in lunar basalts is 80–1700 ppm (e.g., Hauri et al., 2011; Tartèse and Anand, 2013, and references therein; Barnes et al., 2014). Assuming a $\log f O_2$ of IW-2 and hydrogen content of 100–400 ppm for primitive lunar basalts (Tartèse and Anand, 2013), the calculated CH_4 content in silicate melt is up to 50 ppm (Fig. 7). Thus, the degassing of lunar mantle may also have released much more CH_4 than CO_2 into the early atmosphere, as long as a few hundreds ppm water (H) in the primitive lunar basalts. However, it should be noted that the heterogeneous distribution of water in lunar mantle (e.g., Albarède et al., 2014; Robinson and Taylor, 2014) must cause different parts of the lunar mantle to degas carbon with different efficiencies, and extremely dry parts of the lunar mantle may not degas significant quantity of CH_4. Furthermore, these calculated values of CH_4 contents in both lunar and Martian basalts may be maximum because other volatiles such as nitrogen at reduced conditions (Kadik et al., 2011; Li et al., 2013, 2015) may compete for non-hydroxyl hydrogen. However, with 200–600 ppm H and $\log f O_2$ of IW-2 to IW, our experiments indeed show 20–70 ppm CH_4 in silicate melt (see Fig. 7). We also note that the CH_4 contents in natural basaltic melt (12–260 ppm) at 1600 °C, 3 GPa, $\log f O_2$ of IW-0.6 to IW-4.7, and 80–610 ppm H in this study (Fig. 7) are comparable to the CH_4 solubility (52–363 ppm) in a Fe-free, Mg-poor synthetic haplobasalt at 1400–1450 °C, 0.7–3 GPa, $\log f O_2$ of IW-1.4 to IW-4, and 1400–7800 H in Ardia et al. (2013). Future experiments will be required to better understand the effects of temperature, pressure, and melt composition on CH_4 solubility in natural basalt.

5. Conclusions

Our experiments demonstrate:

(1) Carbon solubility in Fe-rich alloy melt is not affected by the presence of 0–5 wt% S but decreases with increasing Si content from 0 to 10 wt%.
(2) Carbon solubility in silicate melt depends on both $f O_2$ and melt water content. The main carbon species in silicate melt at IW-1 < $\log f O_2$ < IW-5 is methane and a fraction of carbon is present as CO_3^{2-} at $\log f O_2$ at least down to IW-0.7.
(3) The $D_C^{metal/silicate}$ ranges from 180 to 4600, decreasing with increasing melt water content and Si content in alloy melt, and decreasing $\log f O_2$ from IW-1.5 to IW-5, where methane or methyl group is the dominant form of carbon in basalt and Si becomes an important light element in Fe-rich alloy melt. The trend of decreasing $D_C^{metal/silicate}$ with decreasing $\log f O_2$ from ~IW-1.5 to IW-5 is in contrast with the trend of increasing $D_C^{metal/silicate}$ with decreasing $\log f O_2$ down to ~IW-1.5 where carbonates continue to be significant fractions of dissolved carbon in basaltic melt (Dasgupta et al., 2013a; Chi et al., 2014). Therefore, in a highly reduced, moderately hydrous MO, a considerable amount of carbon would be retained in the silicate mantle after core-formation; however in a dry MO or if the Earth's carbon was delivered only during late stage of accretion in a relatively oxidized MO (Wood et al., 2013), nearly the entire carbon would be segregated into the core.
(4) Degassing of the post-core formation MO may have released methane into the early planetary atmospheres, and degassing of reduced planetary mantles such as the ones of Mars and the Moon may have released much more methane than carbon dioxide, which helps maintain an early warm atmosphere of Mars.

Acknowledgements

We would like to thank Megan Duncan for help with FTIR analyses, Ray Guillemette for help with electron microprobe analyses, and Brian Monteleone for help with SIMS analyses. We also acknowledge thoughtful comments by two anonymous reviewers and editorial handling of the manuscript by Bernard Marty. This work was supported by NASA grant NNX13AM51G to R.D.

Appendix A. Supplementary material

Supplementary material related to this article can be found online at http://dx.doi.org/10.1016/j.epsl.2015.01.017.

References

Albarède, F., Albalat, E., Lee, C.-T., 2014. An intrinsic volatility scale relevant to the Earth and Moon and the status of water in the Moon. Meteorit. Planet. Sci., 1–10. http://dx.doi.org/10.1111/maps.12331.
Allegre, J.A., Poirier, J.P., Humler, E., Hofmann, A.W., 1995. The chemical composition of the Earth. Earth Planet. Sci. Lett. 134, 515–526.
Ardia, P., Hirschmann, M.M., Withers, A.C., Stanley, B.D., 2013. Solubility of CH_4 in a synthetic basaltic melt, with applications to atmosphere–magma ocean–core partitioning of volatiles and to the evolution of the Martian atmosphere. Geochim. Cosmochim. Acta 114, 52–71.
Bali, E., Audétat, A., Keppler, H., 2013. Water and hydrogen are immiscible in Earth's mantle. Nature 495, 220–223.
Barnes, J.J., Tartèse, R., Anand, M., McCubbin, F.M., Franchi, I.A., Starkey, N.A., Russell, S.S., 2014. The origin of water in the primitive Moon as revealed by the lunar highlands samples. Earth Planet. Sci. Lett. 390, 244–252.
Bouchard, D., Bale, C.W., 1995. Simultaneous optimization of thermochemical data for liquid iron alloys containing C, N, Ti, Si, Mn, S, and P. Metall. Mater. Trans., B 26, 467–484.
Bouhifd, M.A., Jephcoat, A.P., 2011. Convergence of Ni and Co metal–silicate partition coefficients in the deep magma-ocean and coupled silicon–oxygen solubility in iron melts at high pressures. Earth Planet. Sci. Lett. 307, 341–348.
Bouhifd, M.A., Andrault, D., Bolfan-Casanova, N., Hammouda, T., Devidal, J.L., 2013. Metal–silicate partitioning of Pb and U: effects of metal composition and oxygen fugacity. Geochim. Cosmochim. Acta 114, 13–28.
Boujibar, A., Andrault, D., Bouhifd, M.A., Bolfan-Casanova, N., Devidal, J.-L., Trcera, N., 2014. Metal–silicate partitioning of sulphur, new experimental and thermodynamic constraints on planetary accretion. Earth Planet. Sci. Lett. 391, 42–54.
Busigny, V., Cartigny, P., Philippot, P., Javoy, M., 2003. Ammonium quantification in muscovite by infrared spectroscopy. Chem. Geol. 198, 21–31.
Chi, H., Dasgupta, R., Duncan, M., Shimizu, N., 2014. Partitioning of carbon between Fe-rich alloy melt and silicate melt in a magma ocean – implications for the abundance and origin of volatiles in Earth, Mars, and the Moon. Geochim. Cosmochim. Acta 139, 447–471.
Corgne, A., Wood, B.J., Fei, Y., 2008. C- and S-rich molten alloy immiscibility and core formation of planetesimals. Geochim. Cosmochim. Acta 72, 2409–2416.
Dasgupta, R., 2013. Ingassing, storage, and outgassing of terrestrial carbon through geologic time. Rev. Mineral. Geochem. 75, 183–229.
Dasgupta, R., Hirschmann, M.M., 2010. The deep carbon cycle and melting in Earth's interior. Earth Planet. Sci. Lett. 298, 1–13.
Dasgupta, R., Walker, D., 2008. Carbon solubility in core melts in a shallow magma ocean environment and distribution of carbon between the Earth's core and the mantle. Geochim. Cosmochim. Acta 72, 4627–4641.

Dasgupta, R., Buono, A., Whelan, G., Walker, D., 2009. High-pressure melting relations in Fe–C–S systems: implications for formation, evolution, and structure of metallic cores in planetary bodies. Geochim. Cosmochim. Acta 73, 6678–6691.

Dasgupta, R., Chi, H., Shimizu, N., Buono, A., Walker, D., 2013a. Carbon solution and partitioning between metallic and silicate melts in a shallow magma ocean: implications for the origin and distribution of terrestrial carbon. Geochim. Cosmochim. Acta 102, 191–212.

Dasgupta, R., Mallik, A., Tsuno, K., Withers, A.C., Hirth, G., Hirschmann, M.M., 2013b. Carbon-dioxide-rich silicate melt in the Earth's upper mantle. Nature 493, 211–215.

Ding, S., Dasgupta, R., Tsuno, K., 2014. Sulfur concentration of martian basalts at sulfide saturation at high pressures and temperatures – implications for deep sulfur cycle on Mars. Geochim. Cosmochim. Acta 131, 227–246.

Ding, S., Dasgupta, R., Lee, C.-T.A., Wadhwa, M., 2015. New bulk sulfur measurements of Martian meteorites and modeling the fate of sulfur during melting and crystallization – implications for sulfur transport from Martian mantle to crust-atmosphere system. Earth Planet. Sci. Lett. 409, 157–167. http://dx.doi.org/10.1016/j.epsl.2014.10.046.

Duncan, M.S., Dasgupta, R., 2014. CO_2 solubility and speciation in rhyolitic sediment partial melts at 1.5–3.0 GPa – implications for carbon flux in subduction zones. Geochim. Cosmochim. Acta 124, 328–347.

Eggler, D.H., 1976. Does CO_2 cause partial melting in the low-velocity layer of the mantle? Geology 4, 69–72.

Elkins-Tanton, L.T., 2008. Linked magma ocean solidification and atmospheric growth for Earth and Mars. Earth Planet. Sci. Lett. 271, 181–191.

Elkins-Tanton, L.T., 2012. Magma oceans in the inner solar system. Annu. Rev. Earth Planet. Sci. 40, 113–139.

Falloon, T.J., Green, D.H., 1989. The solidus of carbonated, fertile peridotite. Earth Planet. Sci. Lett. 94, 364–370.

Filiberto, J., Dasgupta, R., 2011. Fe^{2+}–Mg partitioning between olivine and basaltic melts: applications to genesis of olivine-phyric shergottites and conditions of melting in the Martian interior. Earth Planet. Sci. Lett. 304, 527–537.

Filiberto, J., Dasgupta, R., 2015. Constraints on the depth and thermal vigor of melting in the Martian mantle. J. Geophys. Res., Planets. http://dx.doi.org/10.1002/2014JE004745.

Filiberto, J., Treiman, A.H., 2009. Martian magmas contained abundant chlorine, but little water. Geology 37, 1087–1090.

Filiberto, J., Dasgupta, R., Kiefer, W.S., Treiman, A.H., 2010. High pressure, near-liquidus phase equilibria of the Home Plate basalt Fastball and melting in the Martian mantle. Geophys. Res. Lett. 37, L13201. http://dx.doi.org/10.1029/12010gl043999.

Gaillard, F., Michalski, J., Berger, G., McLenna, S.M., Scaillet, B., 2012. Geochemical reservoirs and timing of sulfur cycling on Mars. Space Sci. Rev. 174, 251–300.

Genda, H., Abe, Y., 2003. Survival of a proto-atmosphere through the stage of giant impacts: the mechanical aspects. Icarus 164, 149–162.

Halevy, I., Zuber, M.T., Schrag, D.P., 2007. A sulfur dioxide climate feedback on early Mars. Science 318, 1903–1907.

Hauri, E.H., Weinreich, T., Saal, A.E., Rutherford, M.C., Van Orman, J.A., 2011. High pre-eruptive water contents preserved in lunar melt inclusions. Science 333, 213–215.

Herd, C.D.K., Borg, L.E., Jones, J.J., Papike, J.J., 2002. Oxygen fugacity and geochemical variations in the Martian basalts: implications for Martian basalt petrogenesis and the oxidation state of the upper mantle of Mars. Geochim. Cosmochim. Acta 66, 2025–2036.

Hirschmann, M.M., 2012. Magma ocean influence on early atmosphere mass and composition. Earth Planet. Sci. Lett. 341–344, 48–57.

Hirschmann, M.M., Withers, A.C., Ardia, P., Foley, N.T., 2012. Solubility of molecular hydrogen in silicate melts and consequences for volatile evolution of terrestrial planets. Earth Planet. Sci. Lett. 345–348, 38–48.

Holloway, J.R., Pan, V., Gudmundsson, G., 1992. High-pressure fluid-absent melting experiments in the presence of graphite; oxygen fugacity, ferric/ferrous ratio and dissolved CO_2. Eur. J. Mineral. 4, 105–114.

Holzheid, A., Palme, H., Chakraborty, S., 1997. The activities of NiO, CoO and FeO in silicate melts. Chem. Geol. 139, 21–38.

Kadik, A., Pineau, F., Litvin, Y., Jendrzejewski, N., Martinez, I., Javoy, M., 2004. Formation of carbon and hydrogen species in magmas at low oxygen fugacity. J. Petrol. 45, 1297–1310.

Kadik, A.A., Kurovskaya, N.A., Ignat, Y.A., Kononkova, N.N., Koltashev, V.V., Plotnichenko, V.G., 2011. Influence of oxygen fugacity on the solubility of nitrogen, carbon, and hydrogen in FeO–N_2O–SiO_2–Al_2O_3 melts in equilibrium with metallic iron at 1.5 GPa and 1400 °C. Geochem. Int. 49, 429–438.

Karner, J.M., Papike, J.J., Shearer, C.K., McKay, G., Burger, L., 2007. Valence state partitioning of Cr and V between pyroxene-melt: estimates of oxygen fugacity for Martian basalt QUE 94201. Am. Mineral. 92, 1238–1241.

Kawanishi, S., Yoshikawa, T., Tanaka, T., 2009. Equilibrium phase relationship between SiC and a liquid phase in the Fe–Si–C system at 1523–1725 K. Mater. Trans. 50, 806–813.

Lebrun, T., Massol, H., Chassefiere, E., Davaille, A., Marcq, E., Sarda, P., Leblanc, F., Brandeis, G., 2013. Thermal evolution of an early magma ocean in interaction with the atmosphere. J. Geophys. Res., Planets 118, 1155–1176.

Lewis, R.D., Lofgren, G.E., Franzen, H.F., Windom, K.E., 1993. The effect of Na vapor on the Na content of chondrules. Meteoritics 28, 622–628.

Li, Y., Keppler, H., 2014. Nitrogen speciation in mantle and crustal fluids. Geochim. Cosmochim. Acta 129, 13–32.

Li, Y., Wiedenbeck, M., Shcheka, S., Keppler, H., 2013. Nitrogen solubility in upper mantle minerals. Earth Planet. Sci. Lett. 377–378, 311–323.

Li, Y., Huang, R., Wiedenbeck, M., Keppler, H., 2015. Nitrogen distribution between aqueous fluids and silicate melts. Earth Planet. Sci. Lett. 411, 218–228.

Ma, Z., 2001. Thermodynamic description for concentrated metallic solutions using interaction parameters. Metal. Mater. Trans., B 32, 87–103.

Marty, B., 2012. The origins and concentrations of water, carbon, nitrogen and noble gases on Earth. Earth Planet. Sci. Lett. 313–314, 56–66.

McCubbin, F.M., Smirnov, A., Nekvasil, H., Wang, J., Hauri, E., Lindsley, D.H., 2010a. Hydrous magmatism on Mars: a source of water for the surface and subsurface during the Amazonian. Earth Planet. Sci. Lett. 292, 132–138.

McCubbin, F.M., Steele, A., Hauri, E.H., Nekvasil, H., Yamashita, S., Hemley, R.J., 2010b. Nominally hydrous magmatism on the Moon. Proc. Natl. Acad. Sci. USA 107, 11223–11228.

McCubbin, F.M., Hauri, E.H., Elardo, S.M., Vander Kaaden, K.E., Wang, J., Shearer, C.K., 2012. Hydrous melting of the martian mantle produced both depleted and enriched shergottites. Geology 40, 683–686.

McDonough, W.F., 2003. Compositional model for the Earth's core. In: Carlson, R.W. (Ed.), The Mantle and Core. Elsevier–Pergamon, Oxford.

Miettinen, J., 1998. Reassessed thermodynamic solution phase data for ternary Fe–Si–C system. Calphad 22, 231–256.

Morard, G., Siebert, J., Andrault, D., Guignot, N., Garbarino, G., Guyot, F., Antonangeli, D., 2013. The Earth's core composition from high pressure density measurements of liquid iron alloys. Earth Planet. Sci. Lett. 373, 169–178.

Musselwhite, D.S., Dalton, H.A., Kiefer, W.S., Treiman, A.H., 2006. Experimental petrology of the basaltic shergottite Yamato-980459: implications for the thermal structure of the Martian mantle. Meteorit. Planet. Sci. 41, 1271–1290.

Mysen, B.O., Fogel, M.L., Morrill, P.L., Cody, G.D., 2009. Solution behavior of reduced COH volatiles in silicate melts at high pressure and temperature. Geochim. Cosmochim. Acta 73, 1696–1710.

Mysen, B.O., Kumamoto, K., Cody, G.D., Fogel, M.L., 2011. Solubility and solution mechanisms of C–O–H volatiles in silicate melt with variable redox conditions and melt composition at upper mantle temperatures and pressures. Geochim. Cosmochim. Acta 75, 6183–6199.

Nicholis, M.G., Rutherford, M.J., 2009. Graphite oxidation in the Apollo 17 orange glass magma: implications for the generation of a lunar volcanic gas phases. Geochim. Cosmochim. Acta 73, 5905–5917.

O'Neill, H.S.C., Eggins, S.M., 2002. The effect of melt composition on trace element partitioning: an experimental investigation of the activity coefficients of FeO, NiO, CoO, MoO_2 and MoO_3 in silicate melts. Chem. Geol. 186, 151–181.

Rai, N., van Westrenen, W., 2014. Lunar core formation: new constraints from metal–silicate partitioning of siderophile elements. Earth Planet. Sci. Lett. 388, 343–352.

Ricolleau, A., Fei, Y., Corgne, A., Siebert, J., Badro, J., 2011. Oxygen and silicon contents of Earth's core from high pressure metal–silicate partitioning experiments. Earth Planet. Sci. Lett. 310, 409–421.

Righter, K., Yang, H., Costin, G., Downs, R.T., 2008. Oxygen fugacity in the Martian mantle controlled by carbon: new constraints from the nakhlite MIL 03346. Meteorit. Planet. Sci. 43, 1709–1723.

Righter, K., Pando, K., Danielson, L.R., 2009. Experimental evidence for sulfur-rich Martian magmas: implications for volcanism and surficial sulfur sources. Earth Planet. Sci. Lett. 288, 235–243.

Righter, K., King, C., Danielson, L., Pando, K., Lee, C.T., 2011. Experimental determination of the metal/silicate partition coefficients of germanium: implications for core and mantle differentiation. Earth Planet. Sci. Lett. 304, 379–388.

Robinson, K.L., Taylor, G.J., 2014. Heterogeneous distribution of water in the Moon. Nat. Geosci. 7, 401–408. http://dx.doi.org/10.1038/NGEO2173.

Rubie, D.C., Frost, D.J., Mann, U., Asahara, Y., Nimmo, F., Tsuno, K., Kegler, P., Holzheid, A., Palme, H., 2011. Heterogeneous accretion, composition and core–mantle differentiation of the Earth. Earth Planet. Sci. Lett. 301, 31–42.

Sagan, C., Mullen, G., 1972. Earth and Mars: evolution of atmospheres and surface temperatures. Science 177, 52–56.

Shcheka, S.S., Wiedenbeck, M., Frost, D.J., Keppler, H., 2006. Carbon solubility in mantle minerals. Earth Planet. Sci. Lett. 245, 730–742.

Siebert, J., Badro, J., Antonangeli, D., Ryerson, F.J., 2013. Terrestrial accretion under oxidizing conditions. Science 339, 1194–1197.

Sifré, D., Gardes, E., Massuyeau, M., Hashim, L., Hier-Majumder, S., Gaillard, F., 2014. Electrical conductivity during incipient melting in the oceanic low-velocity zone. Nature 509, 81–85.

Sleep, N.H., Zahnle, K., 2001. Carbon dioxide cycling and implications for climate on ancient earth. J. Geophys. Res. 106, 1373–1399.

Stanley, B.D., Hirschmann, M.M., Withers, A.C., 2011. CO_2 solubility in Martian basalts and Martian atmospheric evolution. Geochim. Cosmochim. Acta 75, 5987–6003.

Stanley, B.D., Hirschmann, M.M., Withers, A.C., 2014. Solubility of C–O–H volatiles in graphite-saturated Martian basalts. Geochim. Cosmochim. Acta 129, 54–76.

Stolper, E., 1982. Water in silicate glasses: an infrared spectroscopic study. Contrib. Mineral. Petrol. 81, 1–17.
Tartèse, R., Anand, M., 2013. Late delivery of chondritic hydrogen into the lunar mantle: insights from mare basalts. Earth Planet. Sci. Lett. 361, 480–486.
Tsuno, K., Dasgupta, R., 2011. Melting phase relation of nominally anhydrous, carbonated pelitic-eclogite at 2.5–3.0 GPa and deep cycling of sedimentary carbon. Contrib. Mineral. Petrol. 161, 743–763.
Tsuno, K., Dasgupta, R., 2015. Fe–Ni–Cu–C–S phase relations at high pressures and temperatures – the role of sulfur in carbon storage and diamond stability at mid- to deep-upper mantle. Earth Planet. Sci. Lett. 412, 132–142. http://dx.doi.org/10.1016/j.epsl.2014.12.018.
Tsuno, K., Frost, D.J., Rubie, D.C., 2013. Simultaneous partitioning of silicon and oxygen into the Earth's core during early differentiation. J. Geophys. Res. 40, 66–71.
Tuff, J., Wood, B.J., Wade, J., 2011. The effect of Si on metal–silicate partitioning of siderophile elements and implications for the conditions of core formation. Geochim. Cosmochim. Acta 75, 673–690.
Wade, J., Wood, B.J., 2005. Core formation and the oxidation state of the Earth. Earth Planet. Sci. Lett. 236, 78–95.
Wadhwa, M., 2008. Redox conditions on small bodies, the Moon and Mars. Rev. Mineral. Geochem. 68, 493–510.
Wetzel, D.T., Rutherford, M.J., Jacobsen, S.D., Hauri, E.H., Saal, A.E., 2013. Degassing of reduced carbon from planetary basalts. Proc. Natl. Acad. Sci. USA 110, 8010–8013. http://dx.doi.org/10.1073/pnas.1219266110.
Wood, B.J., Walter, M.J., Wade, J., 2006. Accretion of the Earth and segregation of its core. Nature 441, 825–832.
Wood, B.J., Wade, J., Kilburn, M.R., 2008. Core formation and the oxidation state of the Earth: additional constraints from Nb, V and Cr partitioning. Geochim. Cosmochim. Acta 72, 1415–1426.
Wood, B.J., Li, J., Shahar, A., 2013. Carbon in the core: its influence on the properties of core and mantle. Rev. Mineral. Geochem. 75, 231–250.
Zahnle, K., Schaefer, L., Fegley, B., 2010. Earth's earliest atmosphere. Cold Spring Harb. Perspect. Biol. 2, a004895.
Zhang, Y., Yin, Q.-Z., 2012. Carbon and other light element contents in the Earth's core based on first-principles molecular dynamics. Proc. Natl. Acad. Sci. USA 109, 19579–19583.